Interference between the Modes of an All-Dielectric Meta-atom

David A. Powell*

Nonlinear Physics Centre and Centre for Ultrahigh-bandwidth Devices for Optical Systems (CUDOS), Research School of Physics and Engineering, The Australian National University, Canberra, Australian Capital Territory 2601, Australia

(Received 17 October 2016; revised manuscript received 2 February 2017; published 7 March 2017)

The modes of silicon meta-atoms are investigated, motivated by their use as building blocks of Huygens metasurfaces. A model based on these modes is presented, giving a clear physical explanation of all features in the extinction spectrum. Counterintuitively, this model can show negative contributions to extinction, which are shown to arise from the interference between nonorthogonal modes. The direct and interference contributions to extinction are determined, showing that conservation of energy is preserved. The Huygens condition of matched electric- and magnetic-dipole moments leads to strong forward scattering and suppressed backscattering. It is shown that higher-order modes with appropriate symmetry generalize this condition, leading to multiple bands of directional scattering. The presented results are obtained using a robust approach to find the modes of nanophotonic scatterers, commonly referred to as quasinormal modes. By utilizing an integral formulation of Maxwell's equations, this work avoids the problem of normalizing diverging far fields, which other approaches require. The model and presented results are implemented in open-source code.

DOI: 10.1103/PhysRevApplied.7.034006

I. INTRODUCTION

Dielectric resonators have applications in microwave and optical frequency ranges, including antennas [1] and as building blocks of metamaterials [2–4], particularly impedance-matched Huygens metasurfaces [5]. The results obtained in such structures are typically explained in terms of modes, determined from the fields at peaks or dips in the spectrum. However, these *ad hoc* methods cannot resolve multiple modes which overlap spectrally, nor can they show how each mode contributes to the spectral response. To obtain a complete picture of the physics of such structures, it is necessary to find the modes independently, as eigensolutions satisfying Maxwell's equations with no incident field.

Approximate methods for finding the modes of dielectric resonators are known [6] which usually assume that $\varepsilon \gg 1$. These methods are inaccurate for the moderate values of permittivity available at optical frequencies, and more sophisticated methods are needed to account for radiation effects. Open nanophotonic resonators such as meta-atoms, nanoantennas, and oligomers are typically strongly radiative systems, where loss cannot be treated as a perturbation. In many nanophotonic systems, material dispersion and losses cannot be neglected, further complicating the problem of finding their modes.

In radiating and dissipative systems, the modes have complex frequencies $s_n = j\omega_n + \Omega_n$, corresponding to damped oscillations of the form $\exp(\Omega_n t)\cos(\omega_n t)$, with $\Omega_n < 0$ [using the time convention $\exp(st)$, with $s = j\omega + \Omega$]. The corresponding modal fields $\mathbf{E}_n$ do not possess the orthogonality usually found in the modes of closed systems, and they are commonly referred to as quasinormal modes [7]. They are particularly useful for solving dipole emission problems [8] since they allow a mode volume to be defined for open cavities [9]. A significant practical difficulty is the requirement to normalize a mode with diverging far fields [10].

A different perspective on the modes of scatterers can be found within the microwave-engineering literature [11], originally motivated by time-domain radar problems. By using integral methods to solve Maxwell's equation, only currents on the scatterer need to be solved for, avoiding the need to explicitly handle the diverging far fields. As it is based on finding the singularities of a scattering operator, this approach is referred to as the singularity expansion method (SEM). The field distributions corresponding to these singularities are identical to the quasinormal modes at the complex frequencies of the singularities $j\omega_n + \Omega_n$. The key difference is that, when solving scattering problems on the $j\omega$ axis, the fields in the SEM approach are reconstructed from the dyadic Green's function, which remains finite in the far field. Thus, the SEM avoids the most significant practical disadvantage of quasinormal modes based on fields.

Recently, it has been shown that the singularity expansion method can be applied to meta-atoms and plasmonic resonators [12–14], clearly identifying the modes which contribute to scattering and coupling problems. However, finding all modes within a region of the complex-frequency

*david.a.powell@anu.edu.au

plane requires an iterative procedure with multiple contour integrations [15]. This iteration greatly increases the computational burden, and it remains unclear how robust this procedure is. In addition, it has not yet been demonstrated whether all spectral features can be explained by such a model, particularly the interference between nonorthogonal modes in the extinction spectrum and the suppression of backscattering corresponding to the Huygens condition [16].

In this work, a robust integral approach to finding modes of open resonators is demonstrated for several all-dielectric meta-atoms, based on the singularity expansion method. In contrast to previous works, it is not limited to bodies of rotation [17]. It is shown how this model leads to a clear decomposition of the extinction spectrum of a silicon disk, automatically accounting for interference between the nonorthogonal modes. By performing a vector-spherical-harmonic decomposition of each mode, the unidirectional scattering behavior is explained. It is shown that higher-order modes can also interfere to suppress backscattering, corresponding to the generalized Huygens condition [18]. Examples are also presented of structures with reduced symmetry, leading to bianisotropic and birefringent meta-atoms.

II. MODELING APPROACH

In this work, quantities are described using the time convention $\exp(st)$, with $s = j\omega + \Omega$, so that the imaginary part of the frequency gives the oscillation rate, and the real part gives the decay rate. A frequency-domain function $f(s)$ has a corresponding time-domain function $f(t)$ which can be obtained through the inverse Laplace transform $f(t) = \mathcal{L}^{-1}\{f(s)\}$. Physically observable quantities must be represented by a real function in the time domain; thus, they must satisfy the constraint $f(s^*) = f^*(s)$ in the frequency domain.

A. The modes of an open resonator

An overview of the integral-equation method used to solve Maxwell's equations, based on the surface equivalence principle, is given in Appendix A. This procedure yields a frequency-dependent matrix $\mathbf{Z}(s)$, which describes the response of the scatterer to an arbitrary excitation field. The unknown current vector $\mathbf{I}$ excited by the incident-field vector $\mathbf{V}$ is

$$\mathbf{I}(s) = \mathbf{Z}^{-1}(s) \cdot \mathbf{V}(s). \tag{1}$$

This equation could be solved numerically, as is done in many commercial software packages. More interestingly, it serves as the starting point for developing the model based on modes.

If the matrix $\mathbf{Z}^{-1}$ is singular at the frequency $s_n = j\omega_n + \Omega_n$, then a finite current $\mathbf{I}$ can be supported without requiring any excitation source $\mathbf{V}$. This case is similar to the well-known one with modes in a closed, lossless system, except that, in an open system, mode frequencies must have some finite damping rate Ω_n. The most important singularities are the pole frequencies s_n, where the impedance matrix satisfies the equations

$$\mathbf{Z}(s_n) \cdot \mathbf{I}_n = 0, \qquad \mathbf{K}_n \cdot \mathbf{Z}(s_n) = 0 \tag{2}$$

for nonzero vectors $\mathbf{I}_n$ and $\mathbf{K}_n$. Physically, $\mathbf{I}_n$ corresponds to the current distribution of the mode, and $\mathbf{K}_n$ determines how well the mode is matched to the incident field. Because of geometric symmetry, many modes are degenerate, with several different eigenvectors $\mathbf{I}_n$ and $\mathbf{K}_n$ having the same pole location s_n. For example, the electric-dipole mode of a sphere can be excited by x-, y-, or z-polarized fields, and this mode is triply degenerate.

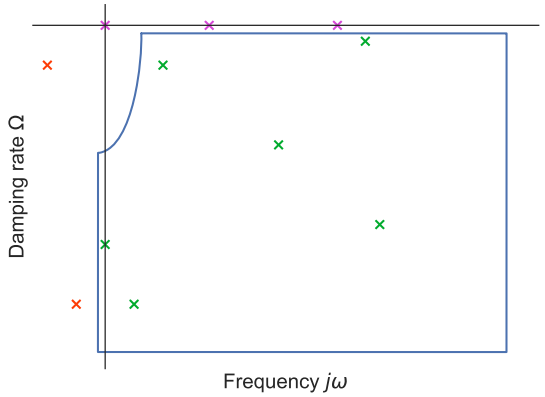

FIG. 1. Modes are found using a contour integration in the complex plane, which yields all enclosed poles $s_n = j\omega_n + \Omega_n$ and their residues with only a single integration. The green crosses represent physical modes with finite radiation damping. The pink crosses indicate spurious internal solutions with no damping. The orange crosses display conjugate modes which can be found by symmetry.

The poles of the impedance matrix are found by a contour integration procedure, details of which are given in Appendix B. Figure 1 illustrates such a contour, which is chosen to encompass all modes which are likely to be of interest. It is offset slightly from the $j\omega$ axis to eliminate any modes which do not couple to incident radiation and hence have $\Omega_n = 0$. The desired radiating modes are shown by green crosses and have $\Omega_n < 0$. Since currents must be real functions in the time domain, for each pole there is a corresponding complex-conjugate pole at $-j\omega_n + \Omega_n$, shown in orange. As the poles and residues are just complex conjugates of those with positive $j\omega_n$'s, they can be found by symmetry and do not need to be included within the contour. Note that some poles are overdamped, with $j\omega_n = 0$, and these poles do not appear in conjugate pairs. The contour incorporates the $j\omega = 0$ axis in order to capture these poles.

In general, no orthogonality relation exists between the mode current vectors $\mathbf{I}_n$ and $\mathbf{K}_n$. As is discussed in Appendix C, orthogonality is not required for this approach. It is shown in Sec. III how this nonorthogonality leads to physically meaningful interference effects.

B. Expanding currents in terms of modes

Once the modes have been found, the current can be solved for arbitrary incident fields,

$$\mathbf{I}(j\omega) = \sum_n \mathbf{I}_n \left(\frac{1}{j\omega - s_n} + \frac{1}{s_n} \right) \mathbf{K}_n \cdot \mathbf{V}(j\omega), \qquad (3)$$

where we consider excitation at physically realizable frequencies on the $j\omega$ axis. The vector $\mathbf{K}_n$ operates on the incident field $\mathbf{V}$ to give its overlap with the mode. The bracketed term accounts for how close the excitation frequency is to the mode's resonant frequency. Note that this polynomial has the correct asymptotic behavior, thus improving the convergence and removing the need to include an entire function contribution [19]. The important result obtained from Eq. (3) is a scalar weighting of each mode's current vector, $\mathbf{I}_n$.

Regardless of whether it is calculated directly from Eq. (1) or as a superposition of modes from Eq. (3), the current vector $\mathbf{I}$ can give the surface current over the entire structure using Eq. (A2). This current distribution could then be used to calculate the total electric and magnetic fields. However, many quantities of physical interest such as scattering, radiation forces, and torques can be calculated directly [20] from the current vector $\mathbf{I}$. The quantity of most interest is the extinction cross section

$$\sigma_{\text{ext}} = \text{Re}[\mathbf{V}^*(j\omega) \cdot \mathbf{I}(j\omega)]\eta_0/|E_0|^2, \qquad (4)$$

giving the total work done by the incident fields on the currents in normalized form. Here, $|E_0|$ is the electric field of the incident plane wave. This quantity can be defined for each mode by substituting the mode's current and its weighting from Eq. (3), yielding

$$\sigma_{\text{ext},n} = \text{Re}[\mathbf{V}^*(j\omega) \cdot \mathbf{I}_n]\eta_0/|E_0|^2. \qquad (5)$$

III. SILICON DISKS

The techniques outlined in Sec. II are now applied to study the scattering behavior of a single silicon-disk metaatom, an important building block of Huygens metasurfaces. Initially, the structure is modeled directly using Eqs. (1) and (4), without considering the modes. The radius is taken as 242 nm, with a height of 220 nm and rounded edges with a radius of 50 nm. The material properties of silicon are obtained by fitting an eight-pole model to the experimental data from Ref. [21]. In Fig. 2, the extinction cross section of the disk is plotted with the solid black line. The incident wave vector is parallel to the axis of the disk.

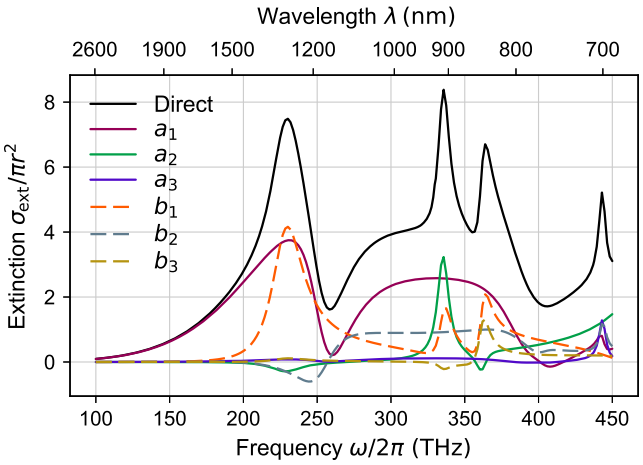

FIG. 2. The extinction cross section of the disk, with direct calculation given by the solid black line. Also shown are contributions from electric- (solid curves) and magnetic- (dashed curves) multipole moments. Curves are shown for different values of multipole order l, summed over all values of the azimuthal index m.

As a first attempt to explain the spectral features, a multipole expansion is also shown in Fig. 2. Details of the expansion are given in Appendix D. Solid lines show the electric-multipole moments a_l, and dashed curves show the magnetic moments b_l. Although the multipoles accurately reproduce the total extinction, there is no direct correspondence between modes and multipoles, with each peak exhibiting contributions from many multipole moments. Furthermore, several multipole moments show peaks and dips at similar locations, but it is unclear if these moments are linked to each other. Therefore, the multipole decomposition is unable to resolve the internal dynamics which are observed in the extinction spectrum. It will be demonstrated that the model based on Eq. (3) can resolve these internal dynamics, showing which modes correspond to each of the spectral features.

A. Modes of the silicon disk

The modes of the silicon disk are found by using the procedure outlined in Sec. II A and Appendix B. Figure 3(a) shows the location of the poles in the complex-frequency plane, with many of them being doubly degenerate. Since currents decay in time as $e^{\Omega t}$, more-highly-damped modes have more-negative values of Ω_n. The schematic of the incident-field orientation is shown in the inset. The modes which most strongly couple to this incident field are indicated with colored markers. The equivalent surface current $\mathbf{J}$ of the first five of these modes is shown in Fig. 4. Since these currents are complex, the plotted vectors give a snapshot of the oscillating current distribution. The divergence $\nabla \cdot \mathbf{J}$ is proportional to the

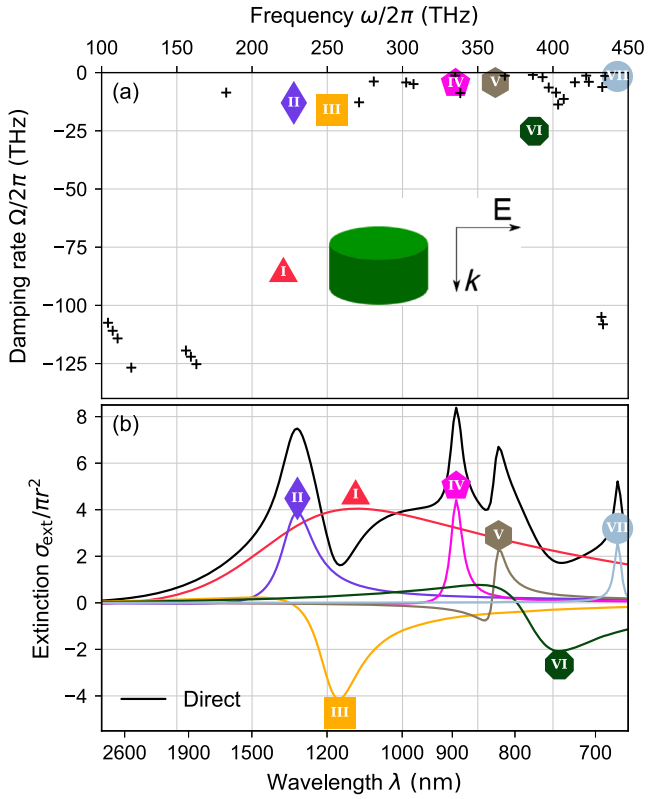

FIG. 3. (a) Complex frequencies of the modes of the silicon disk. Schematic shows the incident plane wave propagating along the disk axis. The colored markers are the modes which couple strongly to the incident wave. (b) Directly calculated extinction (black curve), and contributions from each of the modes. Colors indicate correspondence between the poles and the extinction curves.

equivalent surface charge (and hence to the normal component of the electric field) and is indicated by the shading of the surface. The colors of the markers next to each current distribution correspond to the poles shown in Fig. 3(a). Each mode is also given an arbitrary label in Roman numerals for reference purposes.

We can consider the dielectric disk to be a sphere which has been transformed in a continuous manner, breaking the spherical symmetry. By performing a multipole decomposition of the current for each mode of the disk, we can see which mode of the sphere it is most closely related to. This decomposition is shown in the right column of Fig. 4, where each mode's multipole moments are normalized to the total scattered power, as outlined in Appendix D. In all cases, there is a single dominant multipole moment, although, for higher-order modes, the influence of higher moments becomes more significant. In the following sections, this multipole expansion of the modes is used to explain their contributions to extinction and scattering.

Several of the modes shown in Fig. 4 can be seen to correspond to well-known modes of cylindrical dielectric

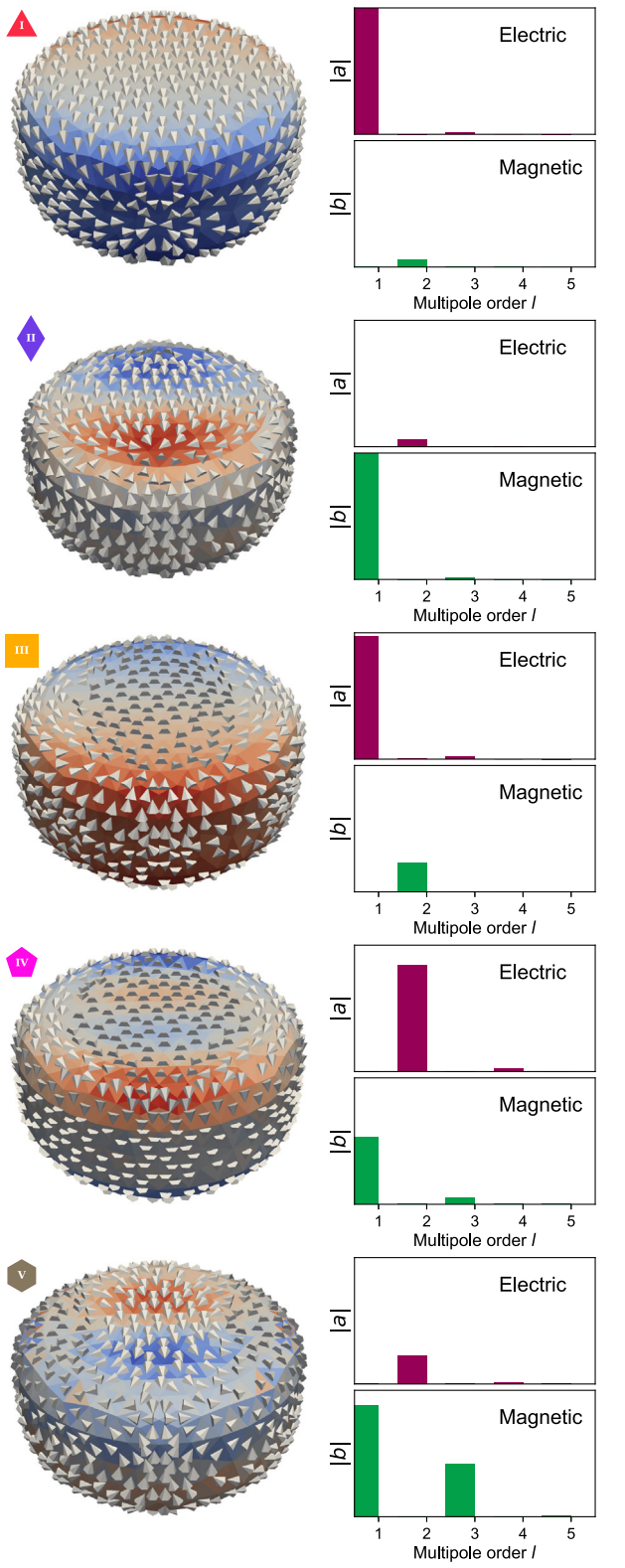

FIG. 4. (Left panels) Modes of the disk, showing equivalent electric surface currents (arrows) and charges (colors). Markers correspond to poles in Fig. 3. (Right panels) Spherical multipoles of each mode, normalized to the total scattered power.

resonators shown in Refs. [3,22,23]. Specifically, mode II is the $HEM_{11\delta}$ mode (also known as $HE_{11\delta}$) and mode III is the $HEM_{12\delta}$ mode (also known as $EH_{11\delta}$). The fundamental dipole-type mode I does not correspond to any of the modes presented in the cited works, but it can be seen to closely resemble the TE_{111} mode of a closed metallic cavity [24]. It is shown below that this mode makes a significant contribution to the response of the disk over a broad frequency range.

B. Extinction spectrum

Figure 3(b) shows the extinction contribution from each of the modes, calculated from Eqs. (3) and (5). The extinction from degenerate pairs of modes has been combined, along with the contribution of their conjugate modes at $-j\omega_n + \Omega_n$. All features in the extinction spectrum can be clearly attributed to the modal contributions. The extinction spectrum for each mode exhibits only a single feature, being a peak and/or dip in the vicinity of its pole frequency ω_n. There is a very clear correspondence between the damping rate Ω_n and the sharpness of the features in the corresponding extinction curve. Note that, for more highly damped modes, there is some shift between the peak and pole frequencies. Such modes couple strongly to the incident field, and therefore the overlap term in Eq. (3) can shift the spectral features away from the natural frequency $j\omega_n$. The accuracy and convergence of this model of extinction is shown in Appendix E.

One of the most striking features of Fig. 3(b) is that several modes show negative contributions to extinction. These contributions are due to the nonorthogonality of the modes, which means that, even if the incident field matches the profile of one mode, it may still excite others. It can be seen that the dip in extinction at around 260 THz can be attributed to a strong negative contribution from mode III, emitting radiation in the forward direction that is in phase with the incident field.

To better illustrate this interference phenomenon, and to confirm that conservation of energy is not violated, the extinction is decomposed into direct terms from each mode, plus interference terms between every pair of modes [25]. This decomposition utilizes an alternative expression for extinction based on the total rate of work done by the excited currents:

$$\sigma_{\text{ext}} = \text{Re}[\mathbf{I}^*(j\omega)\cdot\mathbf{Z}(j\omega)\cdot\mathbf{I}(j\omega)]\eta_0/|E_0|^2. \quad (6)$$

This expression quantifies the total power radiated and dissipated by the currents. Substituting Eq. (3) into Eq. (6), we can decompose the extinction into contributions from each pair of modes:

$$\sigma_{\text{ext},m,n} = \text{Re}[\mathbf{I}_m^*\cdot\mathbf{Z}(j\omega)\cdot\mathbf{I}_n]\eta_0/|E_0|^2. \quad (7)$$

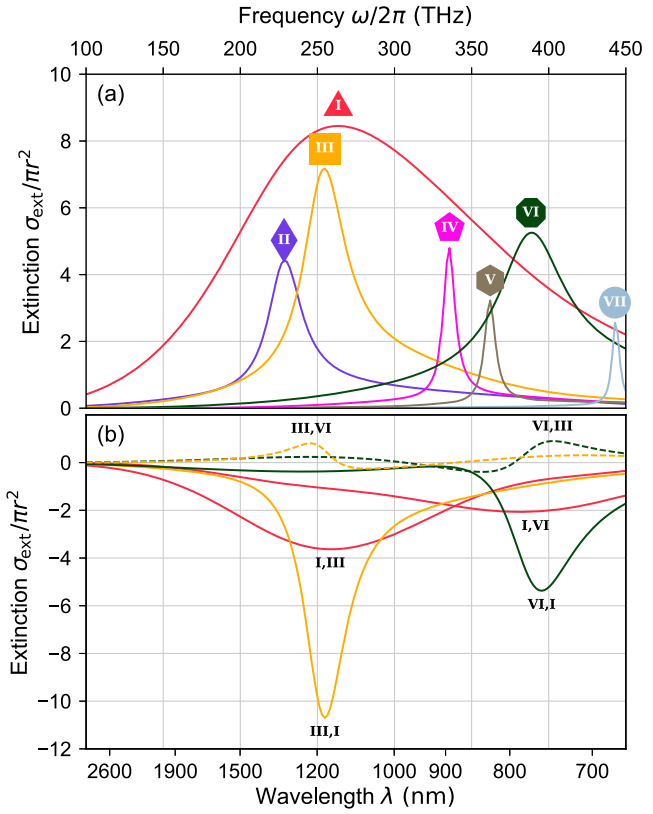

FIG. 5. Interference effects in the extinction spectrum of the silicon disk. (a) Direct extinction contribution $\sigma_{\text{ext},n,n}$ of each mode. (b) The most significant interference terms between modes, $\sigma_{\text{ext},m,n}$, for $m \neq n$ (the solid lines), and selected weaker interference terms (the dashed lines).

Here, $\sigma_{\text{ext},m,n}$ represents the rate of work done on the currents of mode m by those of mode n. The self-terms $m = n$ represent the direct contribution of the mode to scattering and absorption, and they must always be positive in a passive system. These terms are illustrated in Fig. 5(a), and it can be seen that they have much simpler line shapes and are positive, as expected. Thus, if any one of these modes were excited in isolation, there would be no negative contributions to extinction.

The off-diagonal terms $m \neq n$ explicitly show how modes n and m interact with each other. These terms are zero in a closed, lossless system with orthogonal modes and, in an open system, they can also be zero for modes of opposite symmetry, such as modes I and II of the disk studied here. Figure 5(b) shows the most significant interference terms for this structure. The conditions for significant interference between the modes are that they are nonorthogonal, and that they are both excited within the same spectral region. Thus, we see that mode I, with its broad spectral response, interferes with both modes III and VI. On the other hand, although modes III and VI are also nonorthogonal, their limited spectral overlap gives much weaker interference, as is shown by the dashed curves.

Because of passivity requirements, the interference terms between a pair of modes are constrained by the direct terms according to

$$\sigma_{\mathrm{ext},m,n} + \sigma_{\mathrm{ext},m,n} \geq -(\sigma_{\mathrm{ext},m,m} + \sigma_{\mathrm{ext},n,n}). \quad (8)$$

The extinction obtained from Eq. (5) can be understood as the sum of all direct and interference terms acting on mode n,

$$\sigma_{\mathrm{ext},n} = \sum_m \sigma_{\mathrm{ext},n,m}. \quad (9)$$

It should be emphasized that this summation does not need to be performed explicitly, and Eq. (3) yields the total current coefficient for each mode accounting for all interference effects. This expression includes interference between any other modes which have not been explicitly incorporated within the model. Therefore, a sufficient set of modes must be included within the model to have a physically meaningful result; otherwise, Eq. (8) may be violated by some terms not being included.

C. Total scattering

To calculate the total scattering cross section, vector spherical harmonics are used since the total scattering is the incoherent sum of all multipole contributions, given by Eq. (D1). Figure 6 shows the contribution of each multipole coefficient to the scattering cross section. As with the multipole extinction spectrum shown in Fig. 2, the features of the multipole scattering spectra are rather complex, but they can be explained by considering the contributions of different modes. In the wavelength range above 1000 nm, corresponding to the measured range in Ref. [5], it can be seen that the scattering is dominated by the electric-dipole and magnetic-dipole moments a_1 and b_1. The magnetic-dipole moment can be attributed to the resonance of mode II, which has negligible contributions from other moments.

The electric-dipole moment a_1 appears to have two distinct maxima in Fig. 6. From the coefficients shown in Fig. 4, it is clear that only modes I and III contribute to this dipolar scattering. From Fig. 3(b), we can see that mode I has a very broad resonance, while mode III has a much narrower resonance, with a negative contribution to extinction. The result is cancellation of electric-dipole radiation, corresponding to an anapole distribution [26]. This effect is typically explained in terms of a quasistatic electric dipole (a linear current distribution) interfering with a toroidal dipole (a poloidal current distribution). The surface currents shown in Fig. 4 are consistent with this picture; however, the explanation in terms of modes is more general and does not rely on any low-frequency approximations. Indeed, in Ref. [26], it was shown that, for spheres, the anapole distribution is excited when the contributions from the first and second a_1 modes cancel. The situation for the disk is similar, the difference being that the interfering modes I and III have additional contributions from other multipole moments.

D. Directional scattering

For applications in Huygens metasurfaces, the most important attribute of a meta-atom is to have suppressed backscattering and strong forward scattering. This directional scattering is typically achieved by overlapping electric- and magnetic-dipole-type resonances. Figure 7 shows the forward and backward scattering amplitudes, with peaks labeled according to the corresponding resonant modes. The first peak of forward scattering corresponds to the overlap of modes I and III, with almost purely electric-dipole radiation, and mode II, with almost purely magnetic-dipole radiation.

It can also be seen that, at the resonances of modes IV and V, there are additional highly directional scattering

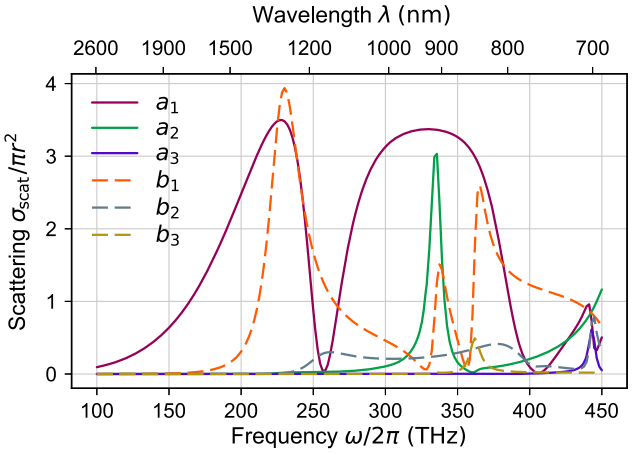

FIG. 6. Contribution of multipole moments to the scattering cross section.

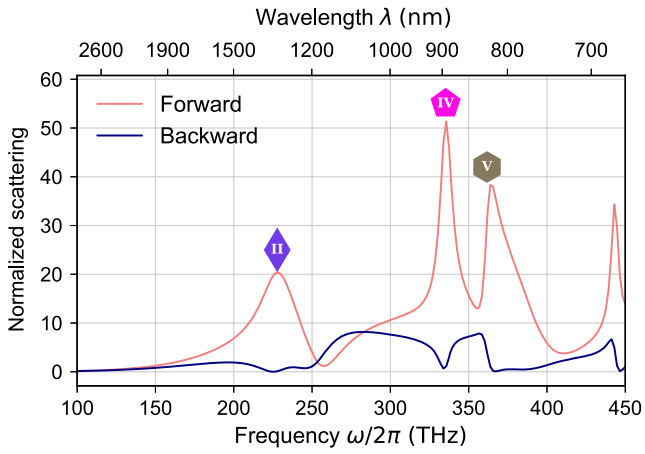

FIG. 7. Forward and backward scattering amplitudes. The markers indicate the modes corresponding to each of the peaks.

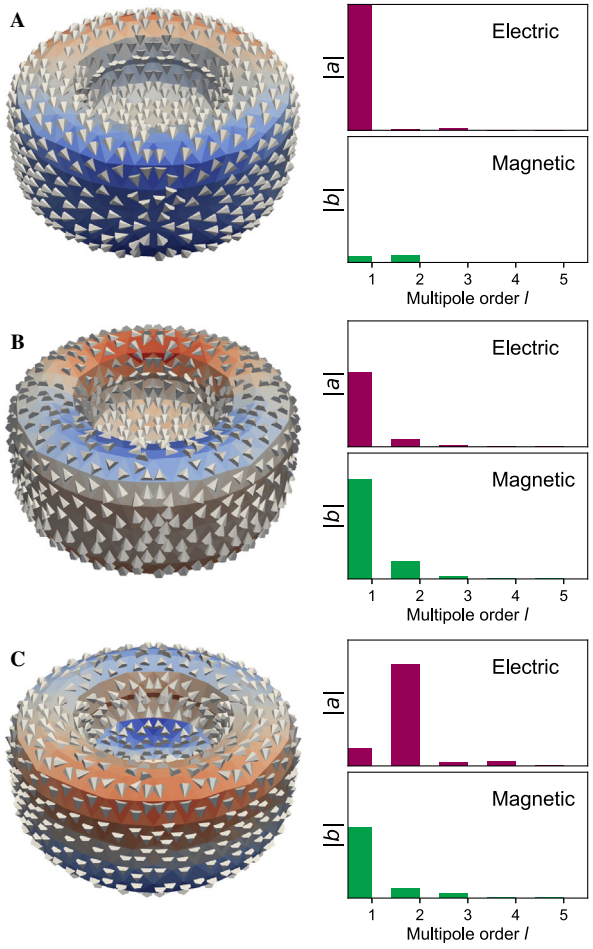

FIG. 8. (Left panels) Modes of a bianisotropic disk with a hole, showing equivalent electric surface currents (arrows), and charges (colors). (Right panels) Spherical multipoles of each mode, normalized to the total scattered power.

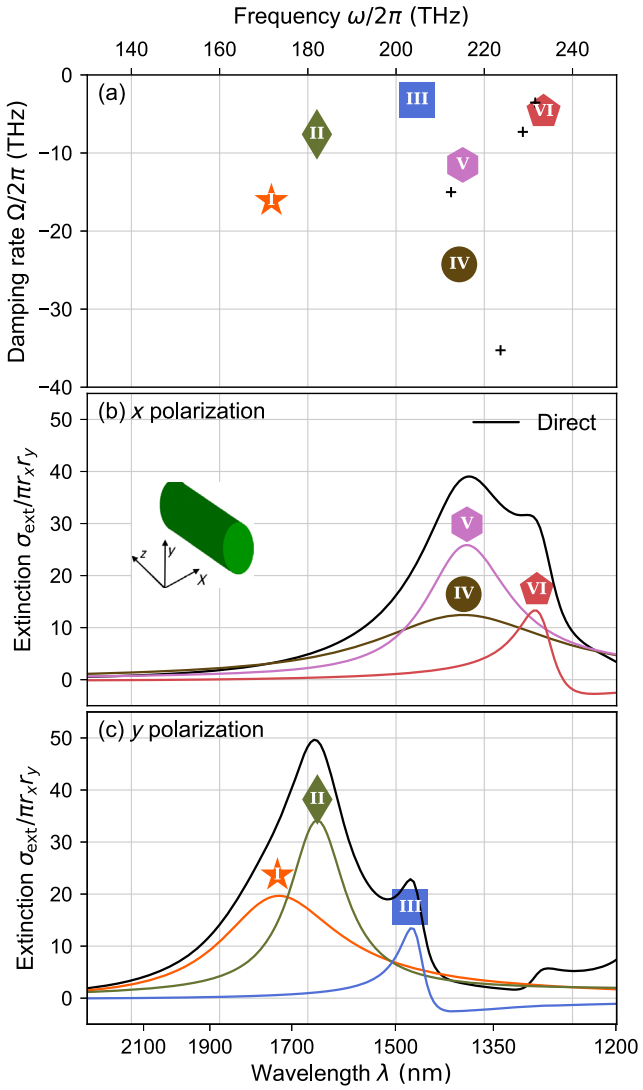

FIG. 9. (a) Location of poles for an elliptical silicon cylinder. (b) Extinction cross section for the incident field polarized along the x axis (the black solid line), along with contributions from the three dominant modes. (Inset) The coordinate convention. (c) Corresponding extinction for an incident field polarized along the y axis.

features, as these modes also overlap with the electric-dipole-type modes I and III. Examining the multipole decompositions in Fig. 4, it can be seen that mode IV is dominated by its electric-quadrupole response, with a significant contribution from its magnetic-dipole response. By contrast, mode V is dominated by its magnetic-dipole response, with lesser contributions from electric-quadrupole and magnetic-octupole moments. It is significant that all of these multipole moments radiate antisymmetric electric fields into the forward and backward directions. When combined with the symmetric electric fields radiated by modes I and III, the backward scattering is canceled, and the forward scattering is enhanced.

Considering the contribution of modes to this directional scattering process, the generalized Huygens condition introduced in Ref. [18] can be reinterpreted as interference between modes of different symmetries. This interpretation suggests that, to optimize this generalized Huygens effect, the meta-atoms should be placed within a homogeneous dielectric environment [5]. A dielectric substrate without a compensating superstrate introduces bianisotropy by coupling modes of opposite symmetry [27].

IV. OTHER STRUCTURES

The technique presented here is quite general and can be applied to a variety of geometries. It is also applicable to a wide range of materials, as discussed in Appendix F. The only significant limitation on geometry is that sharp corners need to be handled carefully since they can cause numerical instability. The simplest solution is to round the edges with some finite radius, and such rounding is expected to occur in experimental samples. The approach makes no assumptions that the structure is smaller than the wavelength;

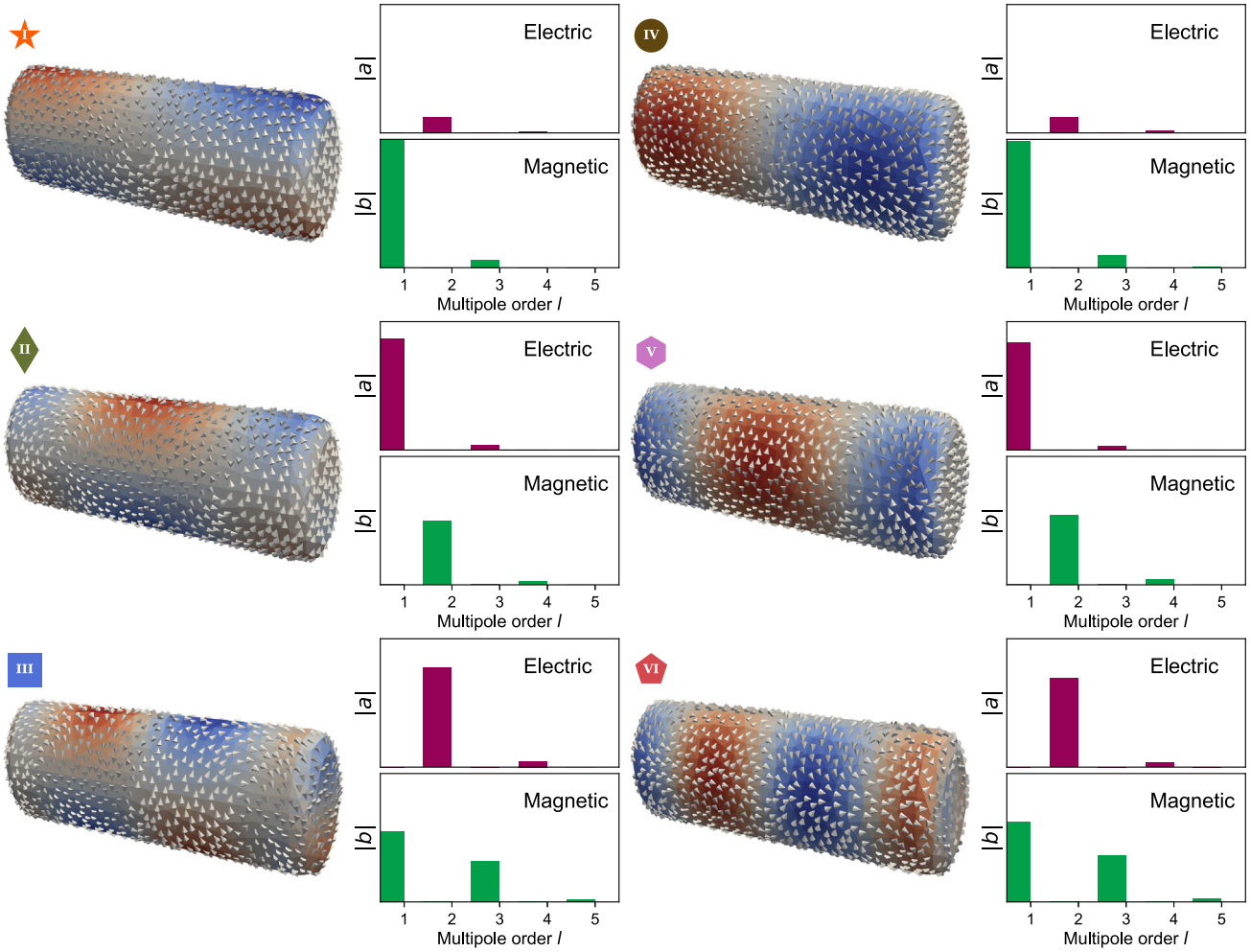

FIG. 10. (Left panels) Modes of the elliptical cylinder, showing equivalent electric surface currents (the arrows) and charges (the colors). Markers correspond to poles in Fig. 9. (Right panels) Spherical multipoles of each mode, normalized to the total scattered power.

however, as the structure becomes large compared to the wavelength, the number of modes typically increases quite dramatically, thus reducing the usefulness of the model. To demonstrate the generality of the method, it is applied to two additional structures.

A. Bianisotropic disk

Recent theoretical [28] and experimental [29] work has shown that placing a hole asymmetrically in a dielectric disk creates an all-dielectric bianisotropic meta-atom. The magnetoelectric polarizability of this structure leads to asymmetric backscattering; however, it is unclear how the various modes of the structure contribute to this process. The structure considered has the same dimensions as the disk studied in Sec. III, with the addition of a hole having a radius of 121 nm and a depth of 110 nm. In Fig. 8, the first three modes of this structure are plotted, along with their multipole expansions. Since the structure is strongly perturbed by the introduction of the hole, these modes can be understood as mixtures of several modes of the regular disk shown in Fig. 4.

Mode A is a predominantly electric-dipole-type mode, and it can be seen that it has a very similar current distribution to mode I of the simple disk. Mode B has quite significant electric- and magnetic-dipole contributions. Examining the current distribution, it can be seen to have circulating current between the front and back faces, similar to mode II of the disk. However, the current in the hole has the opposite direction of that on the rim, leading to a poloidal current distribution which strongly resembles mode III. Mode C is most closely related to mode IV of the simple disk, having a quadrupolar surface charge, but also having significant magnetic-dipole moments.

For all modes, it can be seen that the introduction of the hole has increased the influence of higher-order multipoles, although both modes A and B remain dominated by dipole moments. For the chosen geometric parameters, mode B is the most important contributor to the bianisotropic response. Considering the case where modes A and B

are dominant, mode A suppresses the bianisotropy by adding electric-dipole polarizability which is cross-coupled to a weak magnetic-dipole excitation. Thus, tuning the spectral overlap between these modes enables the net bianisotropy of the structure to be controlled.

B. Elliptical cylinder

Because of their rotational symmetry, the response of disks at normal incidence is identical for both polarizations. For applications in polarization manipulation, anisotropic structures are required. It has been demonstrated [18,30] that long dielectric cylinders of an elliptical cross section allow broadband birefringent metasurfaces to be fabricated, with such applications as phase plates, holograms, and vector beam generators. It can be useful to think of such long meta-atoms as truncated sections of a waveguide, where the transverse variation corresponds to a propagating waveguide mode.

In Fig. 9(a), the poles of an elliptical cylinder are shown, with x and y radii $r_x = 125$ nm and $r_y = 200$ nm, and a length $l = 1100$ nm. These parameters are chosen to approximately overlap several modes for both polarizations, to make forward scattering dominant. The corresponding surface current distributions and multipole moments are shown in Fig. 10. In Figs. 9(b) and 9(c), the extinction is shown for x- and y-polarized incident plane waves, respectively. The inset shows the coordinate convention. As expected, the modes naturally divide into x and y polarizations, determined by the direction of the surface currents on the incident face in Fig. 10.

Examination of Fig. 10 shows that modes I and IV are both magnetic-dipole type, with currents circulating in the plane tangential to $\mathbf{H}$, accompanied by a quadrupolar surface charge distribution. Modes II and V are electric-dipole type, with quite significant magnetic-quadrupole contribution. Finally, modes III and VI are dominated by their electric-quadrupole moments, but they also have quite significant magnetic-dipole and octupole contributions. For each polarization, it can be seen that the higher-order modes have more field maxima in the longitudinal direction, but comparable transverse-field variations. This observation suggests that they arise from a few fundamental transverse waveguide modes, with different longitudinal variations corresponding to Fabry-Perot resonances. From Fig. 9, it is clear that interference effects are considerably less pronounced in this elliptical cylinder than in the disk. This lack of interference makes the structure simpler to analyze but reduces the potential to tailor its spectral response by controlling interference.

V. CONCLUSION

A robust technique based on the singularity expansion method is presented to find the modes of a meta-atom, fully accounting for radiative losses. By solving Maxwell's equations using integral techniques, the problem of normalizing diverging fields is avoided. The technique is applied to a silicon disk, a bianisotropic disk with a hole, and an elliptical cylinder, which are all building blocks of experimentally demonstrated metasurfaces. It is demonstrated that the complicated features of the extinction spectrum can be readily explained in terms of contributions from the modes. Interference between nonorthogonal modes is shown to play a key role, and it is shown how the model automatically accounts for both direct and interference contributions to extinction.

When considering far-field scattering properties, a vector-spherical-harmonic expansion yields an accurate, if somewhat opaque, description. By combining it with the modal analysis, the nature and origin of all scattering features can be elucidated. In the case of the silicon disk, there are several bands of strong forward scattering and suppressed backscattering, corresponding to the generalized Huygens condition. It is shown that each band corresponds to the overlap of modes with odd and even radiation symmetry. The techniques used to find modes and construct models of scatterers are implemented in an open-source code OPENMODES [31], along with notebooks to reproduce all of the results in this paper [32].

ACKNOWLEDGMENTS

The author acknowledges the useful discussions with Andrey Miroshnichenko, Sarah Kostinski, Mingkai Liu, and Yuri Kivshar. This research was funded by the Australian Research Council.

APPENDIX A: INTEGRAL APPROACH TO MAXWELL'S EQUATIONS

Here, a brief outline of the integral approach to solving Maxwell's equations is given. In this work, dielectric objects are considered and are treated through a surface-equivalent problem, with surface-equivalent electric and magnetic currents, $\mathbf{J} = \mathbf{n} \times \mathbf{H}$ and $\mathbf{M} = -\mathbf{n} \times \mathbf{E}$, where $\mathbf{n}$ is the surface normal. These surface currents can be excited by the incident electric or magnetic field, yielding the electric-field integral equation and magnetic-field integral equation, respectively. To yield a stable solution, both of these equations must be combined using chosen weighting coefficients [33]. In this work, the Poggio-Miller-Chang-Harrington-Wu-Tsai form is used [34], which has been established to be positive definite [20,35], as is required for a passive structure. This procedure gives us an operator equation relating equivalent surface currents to the tangential components of the incident fields:

$$\mathcal{Z}(\mathbf{J}, \mathbf{M}) = (\mathbf{E}_{\text{inc}}, \mathbf{H}_{\text{inc}})|_{\tan}. \tag{A1}$$

Equation (A1) is solved numerically using the boundary-element method (also known as the method of moments

[36]). The equivalent surface currents are expanded in terms of a set of basis functions $\mathbf{f}_k(\mathbf{r})$,

$$\mathbf{J}(\mathbf{r}) = \sum_{k=1}^{N} I_k \mathbf{f}_k(\mathbf{r}), \qquad \mathbf{M}(\mathbf{r}) = \frac{1}{\eta_0} \sum_{k=1}^{N} I_{k+N} \mathbf{f}_k(\mathbf{r}), \quad \text{(A2)}$$

where η_0 is the impedance of free space. The current weighting coefficients I_k are assembled into the vector $\mathbf{I}$.

The current expanded in terms of a finite series of basis functions as per Eq. (A2) cannot exactly satisfy Eq. (A1). Therefore, it must be solved by minimizing the residual error with respect to some weighting functions $\mathbf{g}_k$. These functions are applied to the source fields, yielding the source coefficients

$$V_k = \left[\int \mathbf{g}_k(\mathbf{r}) \cdot \mathbf{E}_{\text{inc}}(\mathbf{r}) d^2\mathbf{r}, \ \eta_0 \int \mathbf{g}_k(\mathbf{r}) \cdot \mathbf{H}_{\text{inc}}(\mathbf{r}) d^2\mathbf{r} \right]^T, \quad \text{(A3)}$$

which are assembled into the source vector $\mathbf{V}$. In this work, loop-star functions [37] are used for both basis and testing functions since using the more common Rao-Wilton-Glisson [38] first-order linear functions is found to generate many spurious poles. The weighted operator $\mathcal{Z}$ has a complex expression which can be found in Ref. [34], resulting in the impedance matrix $\mathbf{Z}(s)$.

The response of the system is now described by a matrix equation,

$$\mathbf{V}(s) = \mathbf{Z}(s) \cdot \mathbf{I}(s). \quad \text{(A4)}$$

The impedance matrix $\mathbf{Z}(s)$ is dense and frequency dependent, and it contains all information regarding the response of the scatterer to arbitrary incident fields.

APPENDIX B: POLES OF THE IMPEDANCE MATRIX

It can be seen from Eq. (1) that the singularities of $\mathbf{Z}^{-1}(s)$ will dominate the spectrum of the response, and, using Mittag-Leffler's theorem, the response may be expanded in terms of these singularities [19]. They correspond to solutions which can exist in the absence of a source, and hence they can be used to model the response to an arbitrary incident field. The most important singularities of the impedance matrix are its poles, corresponding to the quasinormal modes of the system. In practice, it may usually be assumed that all poles are of first order [39].

The poles of the impedance matrix are found by the contour-integration procedure of Ref. [40]. First, a pair of matrix integrals $\mathbf{C}_1 = \oint \mathbf{Z}^{-1}(s) ds$ and $\mathbf{C}_2 = \oint s\mathbf{Z}^{-1}(s) ds$ is evaluated about a contour, as shown schematically in Fig. 1. As discussed in Sec. II A, the contour is chosen to enclose only those modes which are likely to be of physical interest. Also note that an arc is used to eliminate the spurious numerical poles which cluster near the origin when using integral operators of the first kind [41].

The mode frequencies and currents are eigenvalues and eigenvectors of $\mathbf{C}_2 \cdot \mathbf{I}_n = s_n \mathbf{C}_1 \cdot \mathbf{I}_n$. A singular value decomposition is used to determine the number of valid solutions to this equation [40], and solving for the corresponding left-eigenvalue problem yields the projectors $\mathbf{K}_n$. This procedure can yield solutions lying both inside and outside the contour, and those falling outside the contour are discarded. The poles and currents are further improved by Newton iteration, then normalized so that $\mathbf{K}_n \cdot \mathbf{Z}'(s_n) \cdot \mathbf{I}_n = 1$. This normalization ensures that the dyadic product of the eigenvectors matches the pole residue, i.e.,

$$\mathbf{Z}(s) = \frac{\mathbf{I}_n \mathbf{K}_n}{s - s_n}, \quad \text{(B1)}$$

in the vicinity of s_n, simplifying the pole expansion.

When solving the structure numerically, the imperfect symmetry of the mesh usually results in some frequency splitting of degenerate modes, so a thresholding procedure is used to group closely spaced poles. The contour-integration and iterative search procedures are found to cope with these nearly degenerate poles without requiring any special handling. Note that it is not necessary to orthogonalize degenerate modes since the method is intrinsically able to account for nonorthogonality, as long as the modes span the full eigenspace.

APPENDIX C: ORTHOGONALITY OF THE MODES

As discussed in Ref. [42], the electric fields of quasinormal modes do not obey the usual orthogonality relationship based on a conjugated inner product, i.e., $\int \mathbf{E}_n^* \cdot \mathbf{E}_m d^3\mathbf{r} \neq \delta_{nm}$. However, they do obey an unconjugated orthgonality relationship, which is utilized in most quasinormal mode formulations [10] for the normalization of modes and the projection of external fields.

By contrast, the current vectors on the scatterer obtained in this work do not exhibit any form of orthogonality. Such orthogonality is not required when working with modal currents since they are normalized by weighting them to match the residue of the pole, as shown in Eq. (B1). In addition to providing the current vector $\mathbf{I}_n$, this approach also yields the correctly normalized projector $\mathbf{K}_n$, which gives the projection of an arbitrary field onto each mode by a simple scalar product, as used in Eq. (3).

It is noted that, in the literature, a number of orthogonal decompositions of the impedance matrix $\mathbf{Z}$ have been presented, most prominently the characteristic-mode analysis [43]. As these mode vectors are real, they exhibit the conventional conjugated orthogonality. However, such decompositions suffer from a number of problems which make them unsuited for physically modeling open

resonators. First, the eigenvalue problem must be solved at each frequency, yielding a different set of current vectors at each frequency. An algorithm is required to track these modes with frequency [44], and they cannot be used to solve time-domain problems.

More significantly, the enforcement of mode orthogonality in an inherently non-Hermitian system results in an artificial set of basis vectors which contain a complex mixture of underlying eigenvectors. This mixing leads to unphysical avoided crossings, whereby the nature of a pair of modes is swapped in some frequency region [45]. The author has observed similar behavior when utilizing other orthogonal decompositions of the impedance matrix, such as the singular value decomposition. In order to reproduce the interference phenomena observed in Fig. 3, it is essential to use the nonorthgonal modes obtained either from the singularity expansion method, or the quasinormal mode approaches.

APPENDIX D: MULTIPOLE DECOMPOSITION

The electric-multipole coefficients a_{lm} and the magnetic-multipole coefficients b_{lm} are computed directly from the surface currents using the formulas from Ref. [46]. Duality allows these formulas to be generalized to include the equivalent magnetic currents through the substitution $\mathbf{J} \to j(1/\eta_0)\mathbf{M}$. The normalization of multipole coefficients from Ref. [47] is used, as this simplifies the expression for the scattering cross section, which is given by

$$\sigma_{\text{scat}} = \frac{\eta_0}{k^2|E_0|^2}\sum_{l=1}^{l_{\max}} |a_l|^2 + |b_l|^2, \tag{D1}$$

where the coefficients include contributions from all values of azimuthal index m:

$$|a_l|^2 = \sum_{m=-l}^{l} |a_{lm}|^2, \qquad |b_l|^2 = \sum_{m=-l}^{l} |b_{lm}|^2. \tag{D2}$$

In Fig. 4, $|a_l|^2$ and $|b_l|^2$ are normalized to their sum, and their square root is plotted since it more clearly shows the smaller contributions. In Fig. 6 these terms are plotted, including the prefactor from Eq. (D1), to give them dimensions of the scattering cross section.

For a plane wave propagating in the z direction, with an incident electric field along the y direction, the extinction cross section is given by [46]

$$\sigma_{\text{ext}} = \frac{\pi}{k^2}\sum_{l=1}^{l_{\max}} \sqrt{2l+1}\left(\left[\sum_{m=-1,1} \text{Im}\{a_{lm}\}\right] + \left[\sum_{m=-1,1} m\text{Im}\{b_{lm}\}\right]\right). \tag{D3}$$

The quantities in square brackets are plotted in Fig. 2, including all of the common prefactors in Eq. (D3). For three terms of the multipole expansion, the extinction plotted in Fig. 2 agrees with the direct calculation to a relative error below 2% for frequencies below 350 THz.

By adapting the formulas from Mie theory [48], forward scattering can be found as

$$W_f = \frac{\pi}{4k^2}\left|\sum_{l=1}^{l_{\max}} \sqrt{2l+1}\sum_{m=-1,1}^{l} a_{lm} + mb_{lm}\right|^2, \tag{D4}$$

while backscattering is given by

$$W_b = \frac{\pi}{4k^2}\left|\sum_{l=1}^{l_{\max}} (-1)^l\sqrt{2l+1}\sum_{m=-1,1}^{l} a_{lm} - mb_{lm}\right|^2. \tag{D5}$$

As losses are low in this system, the total extinction and scattering are approximately equal due to the optical theorem. However, the optical theorem still allows each multipole's contribution to extinction shown in Fig. 2 to be different from its contribution to scattering shown in Fig. 6.

APPENDIX E: ACCURACY OF THE MODAL EXPANSION

To confirm the accuracy of the modal expansion, the directly calculated extinction curve is plotted in Fig. 11 (the solid line), as is the sum of all contributions plotted in Fig. 3(b) (the red dashed line). It can be seen that the agreement is good for frequencies below 250 THz; however, at high frequencies, it becomes poorer. In this curve, the number of poles considered is 28, corresponding to the seven modes studied in Sec. III, each doubly degenerate and with conjugate poles.

To improve agreement, all 145 poles found by the contour-integration process are included, not just the most

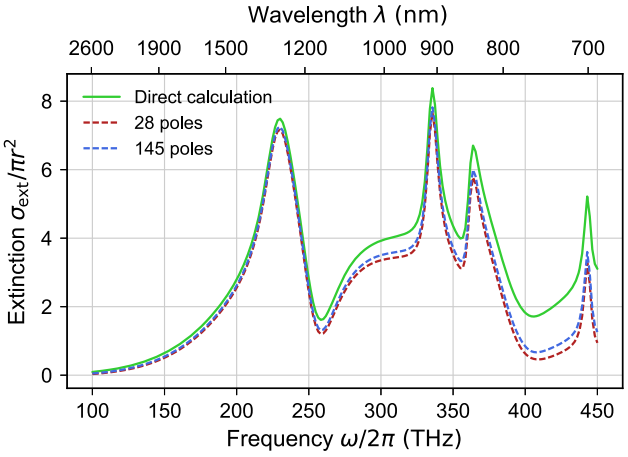

FIG. 11. Accuracy of the extinction calculated from the model including different numbers of modes (the dashed lines), compared with the directly calculated result (the solid line).

significant. In this case, some of the included modes are polarized along the disk axis—and hence are not doubly degenerate—while others are overdamped and hence do not appear in conjugate pairs. Including all of these poles, much better agreement is achieved, as shown by the blue dashed curve. Clearly, a model involving so many parameters is less useful as a design tool; thus, there is an inevitable trade-off between accuracy and the level of insight provided. However, in contrast to simpler approaches based on point dipole or equivalent circuit models, it is possible to control the level of detail which is included within the model by choosing to include or exclude poles.

APPENDIX F: MATERIAL MODELS

Any material may be incorporated into the model, as long as its permittivity (and permeability, if applicable) can be described by a meromorphic function in the complex-frequency plane. This condition corresponds to the permittivity having a real, causal representation in the time domain, and it is exactly the same issue faced when creating material models for use with, e.g., the finite-difference time-domain method. The common material model of a sum of Drude-Lorentz oscillators, or a related approach, can be used [49]. Such material models simultaneously include both dispersion effects, as required by the Kramers-Kronig relations. Except in the case of idealized lossless and nondispersive materials, the material permittivity will have its own poles and zeros in the complex plane. In general, the pole frequencies of a scatterer are influenced both by its geometry and by the poles and zeros of the material permittivity.

It is important to note that the impedance matrix $\mathbf{Z}(s)$ contains terms of the form $\exp(-\gamma_0 r)$, with the complex wave number $\gamma_0 = \sqrt{\varepsilon(s)}(s/c)$. The square root operation results in branch points at the poles and zeros of the permittivity, connected by branch cuts [14,50]. For the material data used in this work, all such branch points occur at frequencies above 800 THz; thus, their contribution is neglected in Eq. (3). The accuracy of the results shown in Fig. 11 confirms that no significant contribution from branch points is missing from the result. The lack of branch points in the frequency range of interest also ensures that the integration contour illustrated in Fig. 1 does not intersect any of the branch cuts. Applying the contour integration in a frequency range of high material dispersion would require choosing the contour carefully to account for all branch cuts.

The surface equivalence approach used in this work is best suited to structures composed of a single material. It can be extended to multimaterial structures by also solving for equivalent surface currents on the internal boundary between materials [51]. For composite particles with a highly complex internal structure, the volume integral approach taken in Ref. [15] may be preferable.

[1] *Dielectric Resonator Antennas*, edited by Kwai Man Luk, Electronic and Electrical Engineering Research Studies Antenna Series Vol. 11 (Research Studies Press, Baldock, England, 2003).

[2] Qian Zhao, Lei Kang, B. Du, H. Zhao, Q. Xie, X. Huang, B. Li, J. Zhou, and L. Li, Experimental Demonstration of Isotropic Negative Permeability in a Three-Dimensional Dielectric Composite, Phys. Rev. Lett. **101**, 027402 (2008).

[3] Akram Ahmadi and Hossein Mosallaei, Physical configuration and performance modeling of all-dielectric metamaterials, Phys. Rev. B **77**, 045104 (2008).

[4] James C. Ginn, Igal Brener, David W. Peters, Joel R. Wendt, Jeffrey O. Stevens, Paul F. Hines, Lorena I. Basilio, Larry K. Warne, Jon F. Ihlefeld, Paul G. Clem, and Michael B. Sinclair, Realizing Optical Magnetism from Dielectric Metamaterials, Phys. Rev. Lett. **108**, 097402 (2012).

[5] Manuel Decker, Isabelle Staude, Matthias Falkner, Jason Dominguez, Dragomir N. Neshev, Igal Brener, Thomas Pertsch, and Yuri S. Kivshar, High-efficiency dielectric Huygens' surfaces, Adv. Opt. Mater. **3**, 813 (2015).

[6] Jean Van Bladel, On the resonances of a dielectric resonator of very high permittivity, IEEE Trans. Microwave Theory Tech. **23**, 199 (1975).

[7] E. Ching, P. Leung, A. Maassen van den Brink, W. Suen, S. Tong, and K. Young, Quasinormal-mode expansion for waves in open systems, Rev. Mod. Phys. **70**, 1545 (1998).

[8] Philip Trøst Kristensen and Stephen Hughes, Modes and mode volumes of leaky optical cavities and plasmonic nanoresonators, ACS Photonics **1**, 2 (2014).

[9] C. Sauvan, J. P. Hugonin, I. S. Maksymov, and P. Lalanne, Theory of the Spontaneous Optical Emission of Nanosize Photonic and Plasmon Resonators, Phys. Rev. Lett. **110**, 237401 (2013).

[10] Philip Trøst Kristensen, Rong-Chun Ge, and Stephen Hughes, Normalization of quasinormal modes in leaky optical cavities and plasmonic resonators, Phys. Rev. A **92**, 053810 (2015).

[11] Carl E. Baum, Emerging technology for transient and broad-band analysis and synthesis of antennas and scatterers, Proc. IEEE **64**, 1598 (1976).

[12] Xuezhi Zheng, V. Volskiy, V. K. Valev, G. A. E. Vandenbosch, and V. V. Moshchalkov, Line position and quality factor of plasmonic resonances beyond the quasi-static limit: A full-wave eigenmode analysis route, IEEE J. Sel. Top. Quantum Electron. **19**, 4600908 (2013).

[13] David A. Powell, Resonant dynamics of arbitrarily shaped meta-atoms, Phys. Rev. B **90**, 075108 (2014).

[14] Jouni Mäkitalo, Martti Kauranen, and Saku Suuriniemi, Modes and resonances of plasmonic scatterers, Phys. Rev. B **89**, 165429 (2014).

[15] Xuezhi Zheng, V. K. Valev, N. Verellen, V. Volskiy, L. O. Herrmann, P. Van Dorpe, J. J. Baumberg, G. A. E. Vandenbosch, and V. V. Moschchalkov, Implementation of the natural mode analysis for nanotopologies using a volumetric method of moments (V-MoM) algorithm, IEEE Photonics J. **6**, 1 (2014).

[16] Carl Pfeiffer and Anthony Grbic, Huygens Surfaces: Tailoring Wave Fronts with Reflectionless Sheets, Phys. Rev. Lett. **110**, 197401 (2013).

[17] A. W. Glisson, D. Kajfez, and J. James, Evaluation of modes in dielectric resonators using a surface integral equation

formulation, IEEE Trans. Microwave Theory Tech. **31**, 1023 (1983).
[18] Sergey Kruk, Ben Hopkins, Ivan I. Kravchenko, Andrey Miroshnichenko, Dragomir N. Neshev, and Yuri S. Kivshar, Invited Article: Broadband highly efficient dielectric metadevices for polarization control, APL Photonics **1**, 030801 (2016).
[19] L. W. Pearson, Evidence that bears on the left half plane asymptotic behavior of the SEM expansion of surface currents, Electromagnetics **1**, 395 (1981).
[20] M. T. H. Reid and S. G. Johnson, Efficient computation of power, force, and torque in BEM scattering calculations, IEEE Trans. Antennas Propag. **63**, 3588 (2015).
[21] Martin A. Green and Mark J. Keevers, Optical properties of intrinsic silicon at 300 K, Prog. Photovoltaics **3**, 189 (1995).
[22] D. Kajfez, A. W. Glisson, and J. James, Computed modal field distributions for isolated dielectric resonators, IEEE Trans. Microwave Theory Tech. **32**, 1609 (1984).
[23] Rajesh K. Mongia and Prakash Bhartia, Dielectric resonator antennas—A review and general design relations for resonant frequency and bandwidth, Int. J. Microwave Millimeter-Wave Comput.-Aided Eng. **4**, 230 (1994).
[24] *Dielectric Resonators*, 2nd ed., edited by Darko Kajfez and Pierre Guillon (Noble Publishing, Atlanta, 1998).
[25] Ben Hopkins, Alexander N. Poddubny, Andrey E. Miroshnichenko, and Yuri S. Kivshar, Revisiting the physics of Fano resonances for nanoparticle oligomers, Phys. Rev. A **88**, 053819 (2013).
[26] Andrey E. Miroshnichenko, Andrey B. Evlyukhin, Ye Feng Yu, Reuben M. Bakker, Arkadi Chipouline, Arseniy I. Kuznetsov, Boris Luk'yanchuk, Boris N. Chichkov, and Yuri S. Kivshar, Nonradiating anapole modes in dielectric nanoparticles, Nat. Commun. **6**, 8069 (2015).
[27] David A. Powell and Yuri S. Kivshar, Substrate-induced bianisotropy in metamaterials, Appl. Phys. Lett. **97**, 091106 (2010).
[28] Rasoul Alaee, Mohammad Albooyeh, Aso Rahimzadegan, Mohammad S. Mirmoosa, Yuri S. Kivshar, and Carsten Rockstuhl, All-dielectric reciprocal bianisotropic nanoparticles, Phys. Rev. B **92**, 245130 (2015).
[29] Mikhail Odit, Polina Kapitanova, Pavel Belov, Rasoul Alaee, Carsten Rockstuhl, and Yuri S. Kivshar, Experimental realisation of all-dielectric bianisotropic metasurfaces, Appl. Phys. Lett. **108**, 221903 (2016).
[30] Amir Arbabi, Yu Horie, Mahmood Bagheri, and Andrei Faraon, Dielectric metasurfaces for complete control of phase and polarization with subwavelength spatial resolution and high transmission, Nat. Nanotechnol. **10**, 937 (2015).
[31] David A. Powell, "OpenModes: An eigenmode solver for open electromagnetic resonators," http://davidpowell.github.io/OpenModes/.
[32] See https://github.com/DavidPowell/DielectricDiskPaper, a repository containing notebooks for reproducing all of the figures in this paper.
[33] Roger F. Harrington, Boundary integral formulations for homogeneous material bodies, J. Electromagn. Waves Appl. **3**, 1 (1989).
[34] P. Ylä-Oijala, M. Taskinen, and S. Järvenpää, Surface integral equation formulations for solving electromagnetic scattering problems with iterative methods, Radio Sci. **40**, RS6002 (2005).
[35] Alejandro W. Rodriguez, M. T. H. Reid, and Steven G. Johnson, Fluctuating-surface-current formulation of radiative heat transfer: Theory and applications, Phys. Rev. B **88**, 054305 (2013).
[36] Walton C. Gibson, *The Method of Moments in Electromagnetics* (Chapman and Hall, Boca Raton, 2008).
[37] Giuseppe Vecchi, Loop-star decomposition of basis functions in the discretization of the EFIE, IEEE Trans. Antennas Propag. **47**, 339 (1999).
[38] S. Rao, Donald R. Wilton, and A. Glisson, Electromagnetic scattering by surfaces of arbitrary shape, IEEE Trans. Antennas Propag. **30**, 409 (1982).
[39] Lennart Marin, Major results and unresolved issues in singularity expansion method, Electromagnetics **1**, 361 (1981).
[40] D. A. Bykov and L. L. Doskolovich, Numerical methods for calculating poles of the scattering matrix with applications in grating theory, J. Lightwave Technol. **31**, 793 (2013).
[41] George W. Hanson and Alexander B. Yakovlev, *Operator Theory for Electromagnetics* (Springer-Verlag, New York, 2002).
[42] P. T. Leung, S. Y. Liu, and K. Young, Completeness and orthogonality of quasinormal modes in leaky optical cavities, Phys. Rev. A **49**, 3057 (1994).
[43] B. K. Lau, D. Manteuffel, H. Arai, and S. V. Hum, Guest editorial theory and applications of characteristic modes, IEEE Trans. Antennas Propag. **64**, 2590 (2016).
[44] E. Safin and D. Manteuffel, Advanced eigenvalue tracking of characteristic modes, IEEE Trans. Antennas Propag. **64**, 2628 (2016).
[45] K. R. Schab, J. M. Outwater, M. W. Young, and J. T. Bernhard, Eigenvalue crossing avoidance in characteristic modes, IEEE Trans. Antennas Propag. **64**, 2617 (2016).
[46] P. Grahn, A. Shevchenko, and M. Kaivola, Electromagnetic multipole theory for optical nanomaterials, New J. Phys. **14**, 093033 (2012).
[47] John David Jackson, *Classical Electrodynamics*, 3rd ed. (John Wiley & Sons, New York, 1999).
[48] Craig F. Bohren and Donald R. Huffman, *Absorption and Scattering of Light by Small Particles* (John Wiley & Sons, New York, 1983).
[49] Minghui Han, R. W. Dutton, and Shanhui Fan, Model dispersive media in finite-difference time-domain method with complex-conjugate pole-residue pairs, IEEE Microwave Wireless Compon. Lett. **16**, 119 (2006).
[50] Masud Mansuripur, Miroslav Kolesik, and Per Jakobsen, Leaky modes of dielectric cavities, Proc. SPIE Int. Soc. Opt. Eng. **9931**, 99310B (2016).
[51] P. Ylä-Oijala and M. Taskinen, Application of combined field integral equation for electromagnetic scattering by dielectric and composite objects, IEEE Trans. Antennas Propag. **53**, 1168 (2005).